

**Efficient biphoton emission in semiconductors by single-photon recycling**Rituraj <sup>1,2,\*</sup>, Shanhui Fan,<sup>2,†</sup> Zhi-Gang Yu,<sup>3</sup> Paul Boieriu <sup>3</sup>, and Srinu Krishnamurthy<sup>3</sup><sup>1</sup>*Ginzton Laboratory, Stanford University, Stanford, California 94305, USA*<sup>2</sup>*Department of Electrical Engineering, Indian Institute of Technology Kanpur, Kanpur, U.P. 208016, India*<sup>3</sup>*Sivananthan Laboratories, Bolingbrook, Illinois 60040, USA*

(Received 25 October 2022; accepted 7 March 2023; published 27 March 2023)

An efficient biphoton emission process in semiconductors can enable the realization of highly tunable lasers, squeezed light sources, and entangled photon pair sources on an integrated platform. We propose a general single-photon recycling scheme to improve the overall efficiency of the typically weak biphoton emission process in a broad class of semiconductor materials. Using a rate-equation-based analysis, we first frame the general design principles and subsequently design a one-dimensional photonic crystal cavity to reach the ideal photon recycling limit for the spontaneously emitted single photons. The cavity is designed with realistic constituent materials to achieve high biphoton output efficiency in the absence of nonradiative recombination channels.

DOI: [10.1103/PhysRevA.107.033521](https://doi.org/10.1103/PhysRevA.107.033521)**I. INTRODUCTION**

Biphoton emission in semiconductors, where an electron-hole pair (or an exciton) recombines, emitting a photon pair, holds the promise of enabling a broad class of semiconductor-based light sources ranging from highly tunable lasers to squeezed light sources and entangled photon pair sources [1–6]. The realization of these light sources on a semiconductor platform is crucial for various applications in light amplification [4,7,8], quantum metrology [9–12], quantum communication [13,14], and quantum information processing [15,16]. As compared to the more commonly used nonlinear optical crystal based implementations [17–19], the semiconductor-based quantum light sources offer unique advantages in terms of mature semiconductor technology, integrated on-chip realization, and enable both electronic injection and optical injection.

Owing to these above-mentioned advantages and following the experimental demonstration of biphoton emission in III-V compound semiconductors, there has been a lot of interest in realizing optoelectronic devices using biphoton emission [1,4,20]. The primary challenge plaguing the development of these devices is the inherent low efficiency and the broadband nature of the biphoton emission process. The biphoton emission in typical direct-band-gap semiconductors is a second-order electron-hole recombination process where the sum frequency of the emitted photon pair is close to the band gap  $\Omega$ . This process has a significantly lower transition rate as compared to the dominant single-photon emission process that emits a photon with frequencies near  $\Omega$ . Thus improving the biphoton emission efficiency is

a fundamental requirement for any further development of biphoton-emission-based optoelectronic or quantum devices.

Here we propose and design a photonic structure which relies upon single-photon recycling to achieve a high biphoton output efficiency. The fundamental idea is to suppress the single-photon emission to free space and to reabsorb the photons emitted via the single-photon emission process to further boost the biphoton emission efficiency. We design a one-dimensional (1D) photonic-crystal-based structure which traps the photons emitted by the single-photon emission process to facilitate their reabsorption. Theoretically, in the ideal case, the proposed structure could achieve a 100% photon recycling efficiency. Equally important, the designed structure enables efficient extraction of photon pairs emitted via the biphoton emission process near frequency  $\Omega/2$  in a narrow angular range and can potentially serve as an efficient source of polarization-entangled photon pairs. We also note that a three-dimensional (3D) photonic crystal with a complete band gap at  $\Omega$  can also suppress the single-photon emission by reducing the photonic density of states to zero [21,22] and thus improve the biphoton emission efficiency. Our proposed structure is inherently different from such a complete band-gap structure and does not significantly alter the total single-photon emission rate but improves the biphoton emission efficiency by preventing the out-coupling of photons, at frequencies near  $\Omega$ , outside the structure and thus having a high photon recycling efficiency. As compared to the 3D photonic crystals, the proposed 1D structure is much simpler to fabricate using the existing semiconductor manufacturing processes.

The paper is organized as follows. We start with a general rate equation analysis in Sec. II to evaluate the biphoton emission efficiency and the effect of single-photon recycling. In Sec. III we present our proposed 1D photonic-crystal-based design. In Sec. IV we discuss simulation results related to single-photon emission and biphoton emission in the designed photonic structure. The conclusions are given in Sec. V.

\*rituraj@iitk.ac.in

†shanhui@stanford.edu

## II. RATE EQUATION ANALYSIS

In this section we model and study a general semiconductor-based light source using semiclassical rate equations [23]. We consider an optically active material with allowed radiative transitions between a group of upper electronic levels and a group of lower electronic levels. In particular, these could either be the conduction and valence bands in a bulk semiconductor material, quantum wells, or the discrete excited- and ground-state energy levels in a collection of quantum dots. We consider the following three processes driving transition of an electron from upper energy levels to the lower energy levels: spontaneous single-photon emission, spontaneous biphoton emission, and nonradiative processes. We ignore both stimulated single and biphoton emission processes, assuming a weak excitation or pump. This assumption is valid when the optical intensity is lower than the saturation intensity for the electronic system, or equivalently, when the excited-state population is negligible as compared to the ground-state population [24–26]. For the transition of an electron from lower electronic levels into upper electronic levels, we consider the following two processes: optical pumping or electronic injection at a constant rate  $E$  and reabsorption of the spontaneously emitted single photons. We ignore the typically weak biphoton absorption process, owing to the weak excitation assumption, which retains the linearity of the rate equations.

The following set of first-order linear differential equations describe the rate of change in the electron and the photon populations as a result of the aforementioned processes:

$$\frac{dn}{dt} = E - \sum_i (A_i^{(1)} n - d_i^{(1)} p_i^{(1)}) - \frac{1}{2} \sum_{i,j} A_{i,j}^{(2)} n - \Gamma n \quad (1)$$

$$\frac{dp_i^{(1)}}{dt} = A_i^{(1)} n - d_i^{(1)} p_i^{(1)} - \gamma_i^{(1)} p_i^{(1)} \quad (2)$$

$$\frac{dp_i^{(2)}}{dt} = \sum_j A_{i,j}^{(2)} n - \gamma_i^{(2)} p_i^{(2)}. \quad (3)$$

Here,  $n$  is the population in the upper electronic levels,  $p_i^{(1)}$  is the number of photons in the optical mode  $i$  around the single-photon emission frequency of approximately  $\Omega$  [the superscript (1) in Eqs. (1)–(3) represents the processes that occur for photons at frequencies near  $\Omega$ ],  $A_i^{(1)}$  is the spontaneous single-photon emission rate into the  $i$ th optical mode,  $d_i^{(1)}$  and  $\gamma_i^{(1)}$  are the absorption and out-coupling rates of photons in the  $i$ th optical mode, respectively,  $p_i^{(2)}$  is the number of photons in the  $i$ th optical mode at biphoton emission frequencies around  $\Omega/2$  [the superscript (2) represents the processes that occur for photons at frequencies around  $\Omega/2$ ],  $A_{i,j}^{(2)}$  is the biphoton emission rate with a single photon each in the optical modes  $i$  and  $j$ , and  $\gamma_i^{(2)}$  is the photon out-coupling rate for the optical mode  $i$  at frequencies corresponding to the biphoton emission process. In the above rate equations it is assumed that there is no optical mode where the photon emission occurs via both the single-photon emission and the biphoton emission processes. This is justified since in direct-band-gap semiconductors, the spontaneous single-photon emission occurs close to the electronic band-gap frequency ( $\Omega$ ), whereas the biphoton emission occurs at photon frequencies smaller

than  $\Omega$ . While this assumption might not be strictly true in materials with a highly broadened single-photon emission spectrum, in such material systems one can still write a similar set of rate equations by ignoring the biphoton emission into the optical modes with both single-photon emission and biphoton emission contribution. This is justified because the single-photon emission rates are typically several orders of magnitude higher than the biphoton emission rates [1–4]. Thus, the above set of rate equations is quite general and should apply to a broad range of material systems.

Before solving these equations to obtain the steady-state solution, we briefly describe here the biphoton emission process in a semiconductor quantum dot. In the biphoton emission process, an electron in the upper energy level ( $|e\rangle$ ) first makes a virtual transition to an intermediate higher energy state ( $|i\rangle$ ), emitting the first photon in the process, and subsequently makes another virtual transition from the intermediate state to the lower energy level ( $|g\rangle$ ), emitting the second photon. Assuming the two virtual transitions to be of electric dipole type, the biphoton emission rate  $A_{p,q}^{(2)}$  as computed from the second-order perturbation theory is given by [2,3],

$$A_{p,q}^{(2)} = \left| \sum_i \frac{\langle g | \boldsymbol{\epsilon}_p(\mathbf{r}_0) \cdot \mathbf{r} | i \rangle \langle i | \boldsymbol{\epsilon}_q(\mathbf{r}_0) \cdot \mathbf{r} | e \rangle}{E_e - E_i - \hbar\omega_q} + \frac{\langle g | \boldsymbol{\epsilon}_q(\mathbf{r}_0) \cdot \mathbf{r} | i \rangle \langle i | \boldsymbol{\epsilon}_p(\mathbf{r}_0) \cdot \mathbf{r} | e \rangle}{E_e - E_i - \hbar\omega_p} \right|^2 \times \frac{2\pi}{\hbar} e^4 \delta(\hbar\Omega - \hbar\omega_p - \hbar\omega_q), \quad (4)$$

where  $\hbar$  is the reduced Planck's constant,  $e$  is the electron charge,  $\mathbf{r}$  is the quantum mechanical position operator for the electron,  $\boldsymbol{\epsilon}_{p/q}(\mathbf{r}_0)$  is the quantized electric field amplitude vector for the optical mode  $p/q$  at the quantum dot position  $\mathbf{r}_0$ ,  $\omega_{p/q}$  is the frequency corresponding to the  $p$ th/ $q$ th optical mode,  $E_e$ ,  $E_i$ , and  $E_g$  are, respectively, the energies associated with the electron states  $|e\rangle$ ,  $|i\rangle$ , and  $|g\rangle$ , and  $\hbar\Omega = E_e - E_g$ . With the understanding that  $A_{p,q}^{(2)}$  is the rate at which the quantum dot emits a photon pair with a single photon in the optical modes  $p$  and  $q$  each, and with the observation  $A_{p,q}^{(2)} = A_{q,p}^{(2)}$  [Eq. (4)], the factor of 1/2 multiplying the biphoton emission term in the rate equation (1) is to avoid double counting.

Now we proceed to solving the rate equations (1)–(3) in the steady-state operation, where the electron and the photon populations in all the modes are time independent. The net photon fluxes from the single-photon emission ( $S_1$ ), and the biphoton emission ( $S_2$ ) processes are computed to be

$$S_1 = \sum_i \gamma_i^{(1)} p_i^{(1)} = \frac{\sum_i A_i^{(1)} (1 + d_i^{(1)}/\gamma_i^{(1)})^{-1}}{\sum_i A_i^{(1)} (1 + d_i^{(1)}/\gamma_i^{(1)})^{-1} + A_2 + \Gamma} E,$$

$$S_2 = \sum_i \gamma_i^{(2)} p_i^{(2)} = \frac{1 - S_1/E}{1 + \Gamma/A_2} E,$$

where  $A_2 = 1/2 \sum_{i,j} A_{i,j}^{(2)}$  is the total biphoton emission rate. From the above expressions, one can also compute the single

and biphoton output efficiencies  $\eta_1$  and  $\eta_2$ , respectively, as follows:

$$\eta_1 = \frac{S_1}{E} = \sum_i \gamma_i^{(1)} p_i^{(1)}$$

$$= \frac{\sum_i A_i^{(1)} (1 + d_i^{(1)} / \gamma_i^{(1)})^{-1}}{\sum_i A_i^{(1)} (1 + d_i^{(1)} / \gamma_i^{(1)})^{-1} + A_2 + \Gamma}, \quad (5)$$

$$\eta_2 = \frac{1}{2} \frac{S_2}{E} = \sum_i \gamma_i^{(2)} p_i^{(2)} = \frac{1 - \eta_1}{1 + \Gamma / A_2}. \quad (6)$$

In the limit of strong photon reabsorption, i.e.,  $A_i^{(1)} \gamma_i^{(1)} / d_i^{(1)} \rightarrow 0 \forall i$ , the single-photon output efficiency  $\eta_1 \rightarrow 0$  and the biphoton output efficiency  $\eta_2$  is enhanced. If the nonradiative recombination rate  $\Gamma$  is also much smaller than the total biphoton emission rate  $A_2$ , the strong photon reabsorption limit results in an ideal biphoton output efficiency ( $\eta_2 = 1$ ). In the next section we will design a photonic structure to achieve the strong photon reabsorption limit by reducing the effective photon out-coupling rate,  $\gamma_{\text{eff},i}^{(1)} \equiv A_i^{(1)} \gamma_i^{(1)} / d_i^{(1)}$ , to zero for all the modes around the single-photon emission frequency  $\Omega$ . We note that the proposed photon-recycling-based scheme to improve the biphoton emission efficiency is quite general in applicability, with the constraint that the photon reabsorption should primarily occur in the optically active medium.

To summarize the general design principles to enhance single-photon recycling, one needs to design a photonic structure around the emitting medium which can suppress the spontaneous single-photon emission into the modes lying inside the escape cone at the medium-air interface, i.e., have a poor extraction efficiency. As we will discuss in the following section, we realize this using a 1D photonic crystal with a band gap for all the photonic modes inside the escape cone to suppress the corresponding density of states to zero at the emission frequency.

### III. PHOTONIC STRUCTURE DESIGN

As suggested by the rate-equation-based analysis in the previous section, it is desirable to reduce the effective photon out-coupling rates for all the optical modes around the single-photon emission frequency  $\Omega$ . For the designed photonic structure to also work for material systems with broadened single-photon emission spectrum (both homogeneous and inhomogeneous broadening), it should prevent photon out-coupling in a broad frequency range. The designed structure should also facilitate an efficient out-coupling of photons emitted via the biphoton emission process in a narrow angular range along a well-defined direction. Additionally, it is also desirable for the designed photonic structure to be simple to fabricate.

To meet all these requirements, we first design a 1D photonic crystal satisfying the design criteria of being an omnidirectional reflector for light incident from air at both frequencies  $\Omega$  and  $\Omega/2$  [27–29]. We then design a Fabry-Pérot cavity resonance at frequency  $\Omega/2$  in the normal direction by introducing a planar defect into an otherwise perfectly periodic photonic crystal [30]. The cavity/defect is designed in such a way that it does not introduce any additional modes

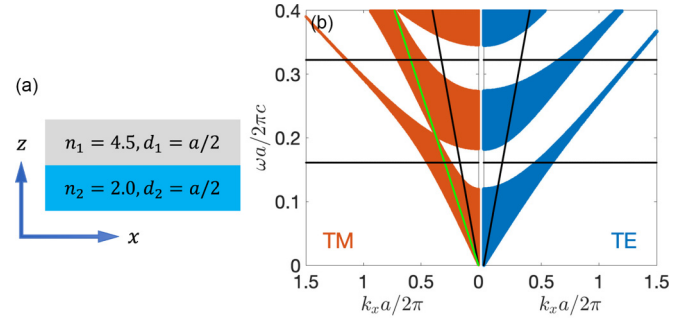


FIG. 1. (a) Unit cell of the 1D photonic crystal with period  $a = 250$  nm, and (b) projected band structure of the photonic crystal showing both transverse magnetic (TM) and transverse electric (TE) polarizations.

around frequency  $\Omega$ . The use of an omnidirectional reflector at  $\Omega$  prevents the out-coupling of photons emitted via the single-photon emission process. The cavity enhances and facilitates an efficient extraction of photons of frequency  $\Omega/2$  along the normal direction emitted via the degenerate biphoton emission process, while the use of an omnidirectional reflector suppresses the output of photons at  $\Omega/2$  at other angles.

Figure 1 shows the unit cell and the projected band structure of the photonic crystal designed for the particular case of  $\lambda_0 = 2\pi c / \Omega = 775$  nm. Note that in this case  $\Omega/2$  corresponds to the telecommunication wavelength  $1.55 \mu\text{m}$ . Throughout the paper we use the convention of the  $z$  axis being along the normal direction. All the photonic structures discussed in this paper are one dimensional, having translational invariance in the  $xy$  plane. The unit cell in Fig. 1(a) has a period of  $a = 250$  nm and is comprised of two layers of equal thicknesses made up of materials with refractive indices  $n_1 = 4.5$  and  $n_2 = 2$ . These values are typically available in materials such as  $\text{MoS}_2$  ( $n_1 \sim 4.5$ ) and boron nitride ( $n_2 \sim 2$ ). The parameters are chosen such that the resulting band structure as shown in Fig. 1(b) satisfies the criteria as outlined above. In the band-structure plot, the red (left) and the blue (right) subplots correspond to the transverse magnetic (TM) and transverse electric (TE) polarizations, respectively. The band structure is only shown for the positive  $k_x$  values, as the negative  $k_x$  part of the band structure is symmetric and can be obtained by taking the mirror image about the vertical ( $\omega$ ) axis. The two horizontal black lines are constant frequency lines at  $\omega = \Omega/2$  and  $\omega = \Omega$ , the two oblique black lines are the light lines in vacuum, and the green oblique line has a slope corresponding to the Brewster angle  $\theta_B = \arctan(n_1/n_2)$  for the media  $n_1$  and  $n_2$ . Within the vacuum light lines there are no optical modes in a finite frequency range around the two frequencies  $\Omega/2$  and  $\Omega$  for both TE and TM polarizations. Thus, a finite lattice of the designed photonic crystal would act as a polarization-insensitive omnidirectional mirror with very high reflection efficiency for light incident from air around these two frequencies [27–29].

Having designed an omnidirectional mirror, we now proceed to next step and design a Fabry-Pérot cavity. Figure 2(a) shows the designed cavity with a resonant mode at frequency  $\Omega/2$  for  $k_x = k_y = 0$ . The central cavity and/or defect layer (outlined by the red rectangle) has thickness  $d_0 = 316.9$  nm,

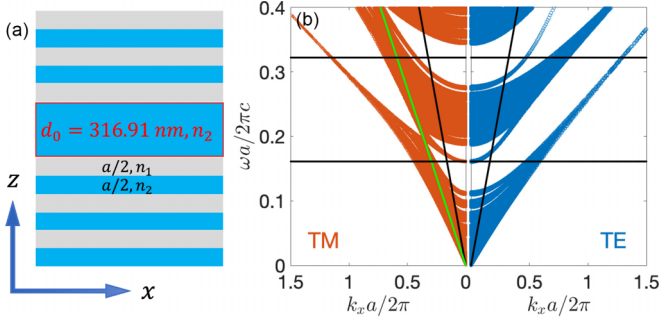


FIG. 2. (a) Schematics of the 1D Fabry-Pérot cavity realized by introducing a defect (outlined by the red rectangle) in the photonic crystal designed previously, and (b) projected band structure of a 1D photonic crystal with the unit cell as shown in (a). The left and right subplots correspond to the TM and TE polarizations, respectively.

refractive index  $n_2 = 2$ , and is surrounded by an omnidirectional mirror on each side. The number of DBR (distributed Bragg reflector) periods ( $n = 2$ ) shown in Fig. 2(a) is for illustration purposes, and we will later study the influence of the number of DBR periods on both the single and biphoton emission properties. To understand the properties of the cavity resonant modes, we compute the band structure of a photonic crystal with the unit cell shown in Fig. 2(a). Figure 2(b) shows the projected band structure with the red (left) and the blue (right) subplots corresponding to the TM and TE polarizations, respectively. Similar to the band-structure plot in Fig. 1(b), the two horizontal black lines are constant frequency lines at  $\omega = \Omega/2$  and  $\omega = \Omega$ , the two oblique black lines are the light lines in vacuum, and the green oblique line has a slope corresponding to the Brewster angle  $\theta_B$  for the media  $n_1$  and  $n_2$ . The band-structure plot in Fig. 2(b) shares many similarities with that of Fig. 1(b) with a few crucial differences arising due to the extra cavity and/or defect layer. By design, the defect layer introduces two degenerate Fabry-Pérot resonant modes (corresponding to TE and TM polarizations) at the frequency  $\Omega/2$  in the normal direction, i.e., at  $k_x = k_y = 0$ , while preserving the omnidirectional gap at frequency  $\Omega$ . The Fabry-Pérot resonances also extend to higher frequencies, but in the off-normal direction ( $k_x \neq 0$ ). As we will see in the next section, the Fabry-Pérot resonances at  $\Omega/2$  help in achieving high biphoton extraction efficiency in a narrow angular range around the normal ( $z$ ) direction, while the omnidirectional gap at frequency  $\Omega$  enhances the single-photon recycling by reducing the effective photon out-coupling rate  $\gamma_{\text{eff},i}^{(1)}$  to zero for all the optical modes around the single-photon emission frequency  $\Omega$ .

#### IV. RESULTS

In this section we discuss the emission characteristics of a quantum dot placed at the center ( $z = 0$  plane) of the designed cavity as shown in Fig. 3(a). We consider a symmetric cavity having an equal number of DBR periods on each side and with the air or vacuum medium outside the finite cavity structure. We model the quantum dot [shown as a red circle in Fig. 3(a)] as a point source assuming the quantum dot size

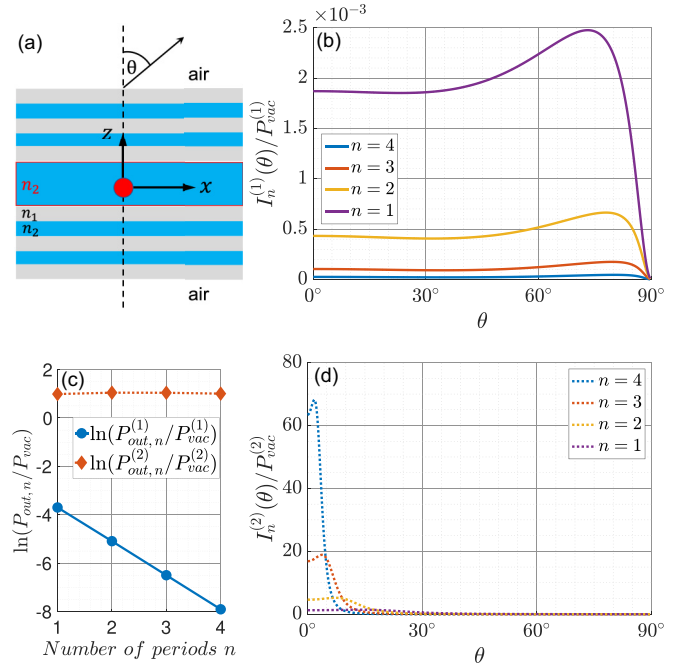


FIG. 3. (a) A quantum dot embedded in a symmetric cavity with  $n$  DBR periods on each side. (b) Normalized angular emission intensity from the dipole rotating at frequency  $\Omega$  for different numbers of DBR periods  $n$ . (c) Normalized total radiated power outside the cavity structure as a function of  $n$  for dipole oscillation frequencies  $\Omega$  (solid curve) and  $\Omega/2$  (dashed curve). (d) Normalized angular emission intensity from the dipole rotating at frequency  $\Omega/2$  for different values of  $n$ .

to be much smaller than the optical wavelength of interest. This assumption is also equally valid for 1D semiconductor quantum-well-based photon sources as the characteristic exciton (electron-hole pair) radius is typically much smaller than the optical wavelengths [31,32]. Even though we consider emission from a single quantum dot, it is implicitly assumed that there is a collection of quantum dots in the infinite  $z = 0$  plane which radiate incoherently, i.e., without fixed phase relation between any two sources. This is crucial for photon recycling, as the single photons emitted by a quantum dot can get reabsorbed and reemitted by another at a different location. As discussed earlier, the quantum dots can either emit a single photon at frequency  $\Omega$  or can emit a photon pair at frequencies  $\omega_1$  and  $\omega_2$  such that  $\omega_1 + \omega_2 = \Omega$ .

#### A. Single-photon emission

We first explore the single-photon emission properties of a quantum dot embedded inside the designed cavity. To study the spontaneous single-photon emission properties of the quantum dot, we consider a classical point dipole source with electric dipole moment phasor  $p_0(\hat{x} + j\hat{y})/\sqrt{2}$  oscillating at single-photon emission frequency  $\Omega$ . The choice of a dipole rotating in the  $xy$  plane is arbitrary, and the following results also apply qualitatively for any random dipole orientation. We first define dipole far-field angular emission intensity in air [ $I_n^{(1)}(\theta, \phi)$ ] as the radiated power per unit solid angle in the direction  $(\theta, \phi)$ , where  $\theta$  and  $\phi$  are the

polar and azimuthal angles, respectively [Fig. 3(a)], and  $n$  is the number of DBR periods on each side of the cavity. The total power emitted outside the structure, i.e., into air, can be computed as  $P_{\text{out},n}^{(1)} = \int_0^{2\pi} d\phi \int_0^\pi d\theta \sin\theta I_n^{(1)}(\theta, \phi)$ . Due to the azimuthal symmetry (rotational invariance about the  $z$  axis), the emission intensity only depends on the polar angle  $\theta$  [ $I_n^{(1)}(\theta, \phi) \equiv I_n^{(1)}(\theta)$ ]. Furthermore, since the cavity has an equal number of DBR periods on top and bottom, the  $z = 0$  plane, the plane the dipole is located in [Fig. 3(a)], is a mirror symmetry plane. This results in identical emission from the top and the bottom of the structure [ $I_n^{(1)}(\theta) = I_n^{(1)}(\pi - \theta)$ ]. These symmetry considerations also apply for the biphoton emission characteristics, which will be discussed later.

Figure 3(b) plots the normalized angular emission intensity for dipole emission into air for different numbers of DBR periods  $n$ . We have normalized the emission intensity with respect to the dipole radiated power in vacuum at frequency  $\Omega$  ( $P_{\text{vac}}^{(1)}$ ). Due to the above-discussed symmetry considerations, in Fig. 3(b) we plot the emission intensity only as a function of polar angle  $\theta$  in the range  $[0, \pi/2]$ . We see that the single-photon emission occurs in a very broad angular range with negligible angular selectivity for all values of  $n$ . Increasing the number of DBR periods suppresses the emission intensity for all angles due to the band-gap effect.

The solid curve in Fig. 3(c) plots the total power radiated outside the structure ( $P_{\text{out},n}^{(1)}$ ) as a function of  $n$  on a semilog scale. As before, we plot the normalized dimensionless quantity  $P_{\text{out},n}^{(1)}/P_{\text{vac}}^{(1)}$ . The power radiated outside the structure can be seen to decrease exponentially as  $n$  increases with  $P_{\text{out},n}^{(1)}$ , decreasing approximately by a factor of 4 with each addition of a DBR period on each side of the cavity, i.e.,  $P_{\text{out},n+1}^{(1)} \approx P_{\text{out},n}^{(1)}/4$ . As discussed in Sec. II, for an ideal photon recycling, the effective photon out-coupling rates  $\gamma_{\text{eff},i}^{(1)} (= A_i^{(1)}\gamma_i^{(1)}/d_i^{(1)})$  for all the optical modes around the single-photon emission frequency  $\Omega$  should be zero, which also implies  $P_{\text{out},n}^{(1)} \rightarrow 0$ . The designed photonic structure approaches this ideal photon recycling limit for sufficiently large  $n$  by reducing the spontaneous single-photon emission rates  $A_i^{(1)}$  to zero for all the optical modes within the vacuum light line around frequency  $\Omega$ . Note that besides the emission into air ( $P_{\text{out},n}^{(1)}$ ), the dipole also emits into the guided modes of the structure, i.e., modes outside the vacuum light line [Fig. 2(b)]. Since by definition, the photon out-coupling rates  $\gamma_i^{(1)}$  for all the guided modes in an infinite structure (infinite in the  $xy$  plane) are zero, for these modes the ideal photon recycling limit is already satisfied irrespective of  $n$ . Thus the designed structure, in the large  $n$  limit, achieves ideal photon recycling for all the optical modes within and outside the vacuum light line around the single-photon emission frequency  $\Omega$ . For the sake of completeness, we also mention here that even though  $P_{\text{out},n}^{(1)}$  becomes vanishingly small in the large  $n$  limit, the total emitted power including the emission into the guided modes of the structure does not decrease and converges to  $2.4 \times P_{\text{vac}}^{(1)}$ , where  $P_{\text{vac}}^{(1)}$  as defined before is the total emitted power from the same dipole when placed in vacuum. The factor 2.4 here is related to the enhancement of the total density of states inside the 1D photonic crystal at the frequency  $\Omega$  (Fig. 2) as compared with the total density of states in vacuum.

## B. Biphoton emission

Having discussed the single-photon emission and the ideal photon recycling limit, we now study the biphoton emission characteristics of the quantum dot. We assume the biphoton emission to occur via a single intermediate state ( $|i\rangle$ ) closest in energy to the excited-state level with the two virtual transitions ( $|e\rangle \rightarrow |i\rangle$ ,  $|i\rangle \rightarrow |g\rangle$ ) being of electric dipole type. We assume the two associated transition dipole moments ( $\langle e|\mathbf{e}r|i\rangle$ ,  $\langle i|\mathbf{e}r|g\rangle$ ) to be oriented in the  $xy$  plane with  $\mathbf{p}_1 = \langle e|\mathbf{e}r|i\rangle = p_1(\hat{x} + \hat{y})/\sqrt{2}$ , and  $\mathbf{p}_2 = \langle i|\mathbf{e}r|g\rangle = p_2(\hat{x} - \hat{y})/\sqrt{2}$ . This corresponds to the two dipoles rotating in opposite directions, i.e., one in a clockwise sense and the other in an anticlockwise sense. This could occur for biphoton transitions between electronic states  $|e\rangle$  and  $|g\rangle$  having equal angular momenta via an intermediate state  $|i\rangle$  with a different angular momentum. For our biphoton emission calculations, we also assume the two transition dipole moments to have equal magnitude, i.e.,  $p_1 = p_2 = p_0$ . As can be seen from Eq. (4), assumptions different from above simply change the biphoton emission rates by an overall scalar factor and do not make a qualitative difference for any of the following discussions. We only study the degenerate biphoton emission at the cavity resonance frequency  $\Omega/2$ .

To compute the biphoton emission rate  $A_{i,j}^{(2)}$  into a pair of optical modes ( $i, j$ ) using Eq. (4), we observe that  $A_{i,j}^{(2)}$  depends on the electric dipole coupling amplitudes into the optical modes  $i$  and  $j$ , which can be obtained from a classical calculation of emission from dipoles  $\mathbf{p}_1$  and  $\mathbf{p}_2$  oscillating at frequency  $\Omega/2$ . The biphoton emission angular intensity distribution and the net biphoton emission rate can be obtained directly from the classical electric dipole radiation. Thus, we first show results corresponding to radiation from dipoles  $\mathbf{p}_1$  and  $\mathbf{p}_2$  placed inside the cavity [in the  $z = 0$  plane as shown in Fig. 3(a)], oscillating at frequency  $\Omega/2$ . The radiation pattern for the two dipoles are identical since  $\mathbf{p}_1 = \mathbf{p}_2^*$ . The dashed curve in Fig. 3(c) shows the total power radiated outside the cavity ( $P_{\text{out},n}^{(2)}$ ) as a function of the number of DBR periods  $n$ . As before, we plot the dimensionless quantity  $\ln(P_{\text{out},n}^{(2)}/P_{\text{vac}}^{(2)})$ , where  $P_{\text{vac}}^{(2)}$  is the total emitted power from the same dipole when placed in vacuum. Unlike the dipole emission at frequency  $\Omega$  [solid curve in Fig. 3(c)], here  $P_{\text{out},n}^{(2)}$  remains almost unchanged as  $n$  is varied. We observe that for  $n \geq 2$ ,  $P_{\text{out},n}^{(2)} \approx 2.8P_{\text{vac}}^{(2)}$ . The factor 2.8 here is related to the enhancement of the total density of states inside the 1D photonic crystal at the frequency  $\Omega/2$  (Fig. 2) as compared with the total density of states in vacuum.

Figure 3(d) shows the normalized angular intensity distribution [ $I_n^{(2)}(\theta, \phi)/P_{\text{vac}}^{(2)} \equiv I_n^{(2)}(\theta)/P_{\text{vac}}^{(2)}$ ] for dipole emission into air for different numbers of DBR periods  $n$ . For better visualization, Fig. 4 shows the 3D far-field dipole radiation pattern  $I_n^{(2)}(\theta, \phi)$  outside the cavity. Here, for a point  $(r, \theta, \phi)$  on the radiation pattern surface, the distance  $r$  from the origin is equal to the normalized angular emission intensity [ $I_n^{(2)}(\theta, \phi)/\max(I_n^{(2)})$ ] in air in the direction  $(\theta, \phi)$ . Figures 3(d) and 4 clearly show that as the number of DBR periods increases, the radiation pattern becomes narrower with the emission primarily occurring in a narrow angular range around the normal direction. In contrast to the dipole

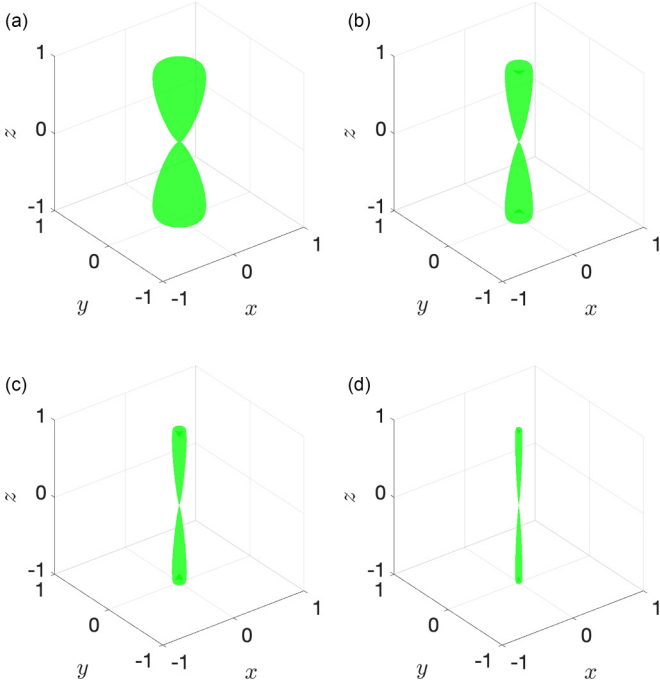


FIG. 4. Far-field radiation patterns for a point dipole oscillating at a frequency  $\Omega/2$  and placed inside a cavity with  $n$  DBR periods on each side for (a)  $n = 1$ , (b)  $n = 2$ , (c)  $n = 3$ , and (d)  $n = 4$ . For a point  $(r, \theta, \phi)$  on the radiation pattern surface, the distance  $r$  from the origin is equal to the normalized angular emission intensity in air  $[I_n^{(2)}(\theta, \phi)/\max(I_n^{(2)})]$ .

radiation at frequency  $\Omega$ , the highly directional nature of dipole emission here is attributed to the presence of the Fabry-Pérot resonance in the normal direction at frequency  $\Omega/2$ . As the number of DBR periods  $n$  is increased, the quality factor of the resonant mode increases and the emission pattern becomes narrower. Even though the angular emission intensity changes with  $n$ , the total power radiated outside the cavity  $P_{\text{out},n}^{(2)} = \int_0^{2\pi} d\phi \int_0^\pi d\theta \sin\theta I_n^{(2)}(\theta, \phi)$  is almost independent of the number of DBR periods for  $n \geq 2$  [Fig. 3(c)]. This phenomenon is a result of resonant dipole emission and is explained using a simple analytical model presented in the Appendix. Furthermore, in the large  $n$  limit, the emission from the dipole  $\mathbf{p}_1$  ( $\mathbf{p}_2$ ) is right (left) circularly polarized. The designed cavity resonances at the frequency  $\Omega/2$  also assist in achieving a high extraction efficiency, which is defined as the ratio of power radiated outside the cavity to the total radiated power ( $\eta_{\text{out},n} = P_{\text{out},n}^{(2)}/P_{\text{tot},n}^{(2)}$ ).  $\eta_{\text{out},n}$  converges to 0.86 for  $n \geq 2$  and is related to the relative ratio of the density of states lying inside the vacuum light line to the total density of states of the structure at the frequency  $\Omega/2$  (Fig. 2). As we will discuss next, the dipole emission into a narrow angular range with high extraction efficiency also leads to narrow biphoton emission pattern with high efficiency. Finally, as a second-order effect, we also note here that the peak emission intensity in Fig. 3(d) occurs at an angle slightly different from the normal direction ( $\theta = 0$ ) and changes with the number of DBR periods  $n$ . This is because the reflection phase for reflection from the 1D photonic crystal surrounding the cavity is a weak function of the angle of incidence and the number of DBR periods  $n$ .

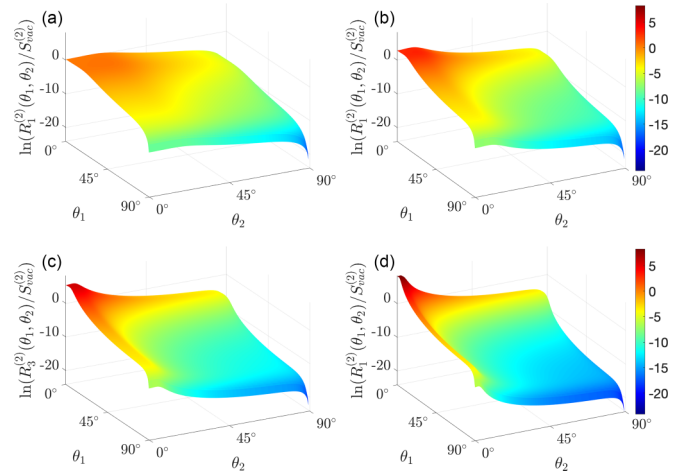


FIG. 5. (a) Angular biphoton emission rate distribution of degenerate photon pairs emitted outside into air by a quantum dot placed inside a cavity with  $n$  DBR periods on each side for (a)  $n = 1$ , (b)  $n = 2$ , (c)  $n = 3$ , and (d)  $n = 4$ .

For the biphoton emission we define a quantity  $R_n^{(2)}(\theta_1, \phi_1, \theta_2, \phi_2)$  as the rate of emission of degenerate photon pairs of arbitrary polarization at frequency  $\Omega/2$  per unit solid angles with one photon each in the directions  $(\theta_1, \phi_1)$  and  $(\theta_2, \phi_2)$ . As per our convention, the subscript  $n$  denotes the number of DBR periods on each side of the cavity. It can be computed from the biphoton emission rates  $A_{i,j}^{(2)}$  as follows. If the index  $i$  for an optical mode in air corresponds to an out-going plane wave with wave vector in the direction  $(\theta_i, \phi_i)$  and polarization  $x_i$ , then the following equation follows:

$$R_n^{(2)}(\theta_1, \phi_1, \theta_2, \phi_2) = \sum_{i,j:\theta_i=\theta_1,\phi_i=\phi_1,\theta_j=\theta_2,\phi_j=\phi_2} A_{i,j}^{(2)}. \quad (7)$$

Experimentally, one can measure  $R_n^{(2)}(\theta_1, \phi_1, \theta_2, \phi_2)$  by counting coincidences on two single-photon detectors placed in the direction  $(\theta_1, \phi_1)$  and  $(\theta_2, \phi_2)$ . Due to azimuthal symmetry,  $R_n^{(2)}(\theta_1, \phi_1, \theta_2, \phi_2)$  is independent of  $\phi_1$  and  $\phi_2$  for  $|\phi_1 - \phi_2| \in (0, 2\pi)$  and thus  $R_n^{(2)}(\theta_1, \phi_1, \theta_2, \phi_2) \equiv R_n^{(2)}(\theta_1, \theta_2)$ . Additionally, since photons are identical particles,  $R_n^{(2)}(\theta_1, \theta_2) = R_n^{(2)}(\theta_2, \theta_1)$ . Figure 5 plots  $R_n^{(2)}(\theta_1, \theta_2)$  for different numbers of DBR periods  $n$ . We plot here the normalized biphoton emission intensity  $R_n^{(2)}(\theta_1, \theta_2)/S_{\text{vac}}^{(2)}$  on a log scale, where  $S_{\text{vac}}^{(2)}$  is the total biphoton emission rate when the quantum dot is placed in vacuum. Similar to the dipole emission pattern at frequency  $\Omega/2$  [ $I_n^{(2)}(\theta, \phi)$ ] as shown in Fig. 4, the angular distribution of biphoton emission also gets narrower as  $n$  increases. The maximum biphoton emission intensity is observed close to the normal direction ( $\theta_1, \theta_2 \rightarrow 0^\circ$ ), and the minimum biphoton emission intensity occurs close to the glancing angle ( $\theta_1, \theta_2 \rightarrow 90^\circ$ ). The maximum biphoton emission intensity can be seen to increase exponentially as the number of DBR periods  $n$  is increased. In the large  $n$  limit, the two emitted photons are completely circularly polarized with opposite polarizations and  $R_n^{(2)}(\theta_1, \phi_1, \theta_2, \phi_2) \propto I_n^{(2)}(\theta_1, \phi_1)I_n^{(2)}(\theta_2, \phi_2)$ . Thus, a large dipole emission intensity in a narrow angular range around the normal direction as realized by the cavity design here also helps in achieving a

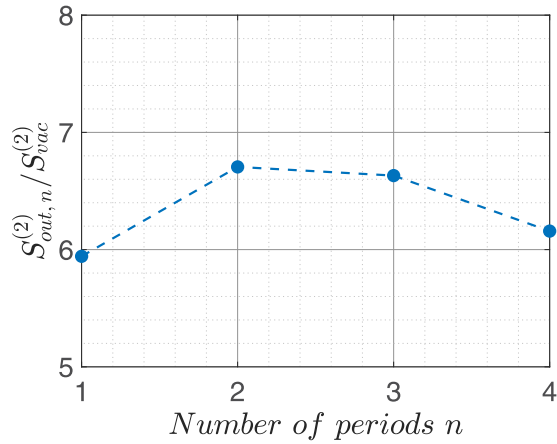


FIG. 6. Total degenerate biphoton emission rate into air by a quantum dot placed inside a cavity with  $n$  DBR periods on each side.

large biphoton emission rate in an even narrower range of angles around the normal direction.

Finally, in Fig. 6 we plot the normalized total biphoton emission rate  $S_{out,n}^{(2)}/S_{vac}^{(2)}$ , where  $S_{out}^{(2)} = \int_0^{2\pi} d\phi_1 \int_0^{2\pi} d\phi_2 \int_0^\pi d\theta_1 \sin\theta_1 \int_0^\pi d\theta_2 \sin\theta_2 R_n^{(2)}(\theta_1, \phi_1, \theta_2, \phi_2)$  is the total biphoton emission rate with both the photons being emitted outside the structure. The Fabry-Pérot resonance at frequency  $\Omega/2$  can be seen to enhance the total rate of biphoton emission outside the cavity by more than 500% as compared to the biphoton emission rate in vacuum. Furthermore, the total biphoton emission rate does not vary appreciably as the number of DBR periods is changed.

Thus the designed resonant cavity enhances the degenerate biphoton emission and makes it highly directional, with both the photons coming out in the normal direction with opposite polarization. For the case of a symmetric cavity as considered here, there is an equal chance for the photons to get emitted either from the top or from the bottom of the cavity. Thus there is a 50% probability for the degenerate biphoton emission to occur with one of the photons emitted in the upward normal direction and the other photon coming out in the downward normal direction. As the only constraint is for the two photons to have opposite polarization, the upward and the downward emitted photons are therefore polarization entangled. Hence the proposed structure can potentially serve as an efficient source of degenerate polarization-entangled photon pairs. As a final remark, we also note that the designed structure also allows for nondegenerate biphoton emission, with at least one of the photons being emitted into the guided modes of the structure which exist at all the frequencies [Fig. 2(b)].

## V. FINAL REMARKS

The geometry of the designed 1D photonic-crystal-based biphoton source is essentially similar to widely employed layered quantum well structures in semiconductors that can be fabricated using various deposition and crystal growth techniques. The optically active (photon-emitting) layer can either be a thin planar layer of a direct-band-gap semiconductor or a collection of semiconductor quantum dots distributed in a plane inside the designed cavity. For efficient photon

recycling, the band gap of the materials constituting the DBR mirrors of the cavity needs to be larger than the band gap of the optically active layer. Besides making metal contacts for electron injection into the optically active layer, the proposed design does not need any complex lithography steps and thus is simple to fabricate.

In summary, we showed that photon recycling could potentially boost the efficiency of the inherently weak biphoton emission process in semiconductors. We also designed a one-dimensional photonic-crystal-based structure to achieve the ideal photon recycling limit and thus a high biphoton output efficiency. The proposed structure is simple to fabricate, is suitable for a broad class of semiconductor materials, and could potentially lead to realization of entangled photon pair sources, squeezed light sources, and highly tunable biphoton-emission-based lasers, all integrated on the same on-chip platform.

## ACKNOWLEDGMENT

The work reported here was supported by the Sivananthan Laboratories, Inc.

## APPENDIX: DIPOLE EMISSION IN PLANAR STRUCTURES

### 1. Methods

All the photonic band structure and the classical dipole emission calculations were performed using the standard transfer matrix method (TMM). To prevent the numerical field amplitude singularities arising from the TMM method for dipole emission into the guided modes of the structure, a thin lossy layer was artificially introduced, and a convergence test was performed for both the dipole emission into air and into the guided modes [33–35].

### 2. Resonant dipole emission inside a 1D cavity

We consider the dipole-cavity system shown in Fig. 3(a) and compute the power radiated into the uniform medium (air) outside the structure. We evaluate the emission from the electric dipole  $\mathbf{p}_1$  oscillating at the resonant frequency of the 1D cavity  $\omega_0 = \Omega/2$ . Nevertheless, the following analysis is general and can be applied for resonant dipole emission inside any arbitrary 1D structure. From the band-structure plot for an infinite periodic cavity structure shown in Fig. 2(b), we observe that there is a single mode each for the TE and TM polarizations around frequency  $\Omega/2$  inside the vacuum light line. Since only the modes inside the vacuum light line contribute to the radiation extracted outside the cavity, we only need to consider these two modes. These two modes correspond to the two Fabry-Pérot resonances in our finite cavity structure with sufficiently large number of DBR periods ( $n \geq 2$ ). As discussed before, the Fabry-Pérot resonances are in the normal direction [ $\mathbf{k}_{\parallel} = (k_x, k_y) = (0, 0)$ ] at the frequency  $\Omega/2$  and extend to higher frequencies in the off-normal directions.

Considering a large volume  $V = L \times L \times L$  enclosing the cavity, all the propagating electromagnetic modes in air can be expressed as a linear combination of plane waves indexed by the incident wave vector in air  $\mathbf{k} \equiv (\mathbf{k}_{\parallel}, k_z)$  and polarization

$u \in \{s, p\}$  as follows:

$$\mathbf{E}_k^u(\mathbf{r}) = \begin{cases} \frac{1}{\sqrt{V}} [\hat{\mathbf{u}}_k \exp(j\mathbf{k} \cdot \mathbf{r}) + r_k \hat{\mathbf{u}}_{k_-} \exp(j\mathbf{k}_- \cdot \mathbf{r})], & \text{for } k_z z < 0 \text{ \& } |z| > D_n/2 \\ \frac{1}{\sqrt{V}} t_k \exp(j\mathbf{k} \cdot \mathbf{r}), & \text{for } k_z z > 0 \text{ \& } |z| > D_n/2, \end{cases} \quad (\text{A1})$$

where  $\mathbf{E}_k^u$  is the electric field phasor,  $\mathbf{k}_- = (\mathbf{k}_\parallel, -k_z)$  is the wave vector of the reflected wave,  $D_n$  is the total thickness of the cavity structure with  $n$  DBR periods on each side,  $\hat{\mathbf{u}}_k$  and  $\hat{\mathbf{u}}_{k_-}$  are the unit electric field polarization vectors for a  $u$ -polarized plane wave propagating in the  $\mathbf{k}$  and  $\mathbf{k}_-$  directions, respectively, and  $r_k$  and  $t_k$  are the reflection and transmission coefficients, respectively.

To compute the dipole emission, we need the field amplitudes at the dipole position ( $\mathbf{r} = \mathbf{0}$ ), which is inside the medium with refractive index  $n_0$ . For a wave incident at angle  $\theta_v = \cos^{-1}(k_z/k)$  from air, the fundamental Fabry-Pérot resonance occurs at frequency  $\omega_\theta \approx \omega_0/|\cos(\theta)|$ , where  $\theta = \sin^{-1}[\sin(\theta_v)/n_0]$  is the angle of refraction inside the medium  $n_0$ . All the modes inside the vacuum light line lie in the range  $\theta \in R = [0, \theta_c] \cup [\pi - \theta_c, \pi]$ , where  $\theta_c = \sin^{-1}(1/n_0)$  is the critical angle in the medium  $n_0$ . At resonance one has  $r_k = 0$  and  $|t_k| = 1$ . Since the dipole plane  $z = 0$  is a mirror symmetry plane, at the fundamental Fabry-Pérot resonant frequency, the electric field maximum occurs in the  $z = 0$  plane. Around the Fabry-Pérot resonant frequency, the maximum electric field amplitude can be approximated by a Lorentzian function as

$$\|\mathbf{E}_k^u(z=0)\|^2 = \frac{1}{V} \frac{1}{\pi Q_\theta^u n_0} \frac{\omega_\theta^2}{[\omega_k - \omega_\theta]^2 + [\omega_\theta/(2Q_\theta^u)]^2}, \quad (\text{A2})$$

where  $\omega_k = c|\mathbf{k}|$  is the frequency,  $c$  is the speed of light in vacuum, and  $Q_\theta^u$  is the quality factor for the Fabry-Pérot resonance along the direction  $\theta \in R$ . Now the power radiated into these resonant modes can be evaluated by the classical expression [36]

$$P_{\text{out},n}^{(2)} = \frac{\pi \omega_0^2}{4\epsilon_0} \sum_{k,u} |\mathbf{p}_1 \cdot \mathbf{E}_k^u(\mathbf{0})|^2 \delta(\omega_k - \omega_0) = \frac{\pi \omega_0^2 p_0^2}{4\epsilon_0} \sum_k \frac{\|\mathbf{E}_k^s(\mathbf{0})\|^2 + \cos^2(\theta) \|\mathbf{E}_k^p(\mathbf{0})\|^2}{2} \delta(\omega_k - \omega_0). \quad (\text{A3})$$

For a simple first-order model, we assume that the quality factor for the Fabry-Pérot resonances is identical across all the angles and for both the polarizations and only depends on the number of DBR periods  $n$ . From Eqs. (A2) and (A3), substituting  $Q_\theta^u = Q$ , and taking the continuum limit as  $V \rightarrow \infty$ , we get

$$\begin{aligned} P_{\text{out},n}^{(2)} &= \frac{\omega_0^2 p_0^2}{32\epsilon_0 \pi^2} \int d^3\mathbf{k} \frac{1 + \cos^2(\theta)}{2} \frac{1/(\pi Q n_0)}{(\omega_k/\omega_0 - 1)^2 + [1/(2Q)]^2} \delta(\omega_k - \omega_0) \\ &= \frac{\omega_0^2 p_0^2}{32\epsilon_0 \pi^2} \int_0^\infty dk \int_0^\pi d\theta_v \int_0^{2\pi} d\phi k^2 \sin(\theta_v) \frac{1 + \cos^2(\theta)}{2} \frac{1/(\pi Q n_0)}{(\omega_k/\omega_0 - 1)^2 + [1/(2Q)]^2} \delta(\omega_k - \omega_0) \\ &= \frac{\omega_0^4 p_0^2}{16\epsilon_0 \pi c^3} \int_0^\pi d\theta_v \sin(\theta_v) \frac{1 + \cos^2(\theta)}{2} \frac{1/(\pi Q n_0)}{(\omega_0/\omega_\theta - 1)^2 + [1/(2Q)]^2}. \end{aligned} \quad (\text{A4})$$

Now using  $\omega_\theta = \omega_0/|\cos \theta|$  and substituting a  $\delta$  function for the Lorentzian function in the limit of large  $Q$ ,

$$P_{\text{out}}^{(2)} = \frac{\omega_0^4 p_0^2}{16\pi \epsilon_0 c^3 n_0} \int_0^\pi d\theta_v \sin(\theta_v) [1 + \cos^2(\theta)] \times \delta[\cos(\theta) - 1] \quad (\text{A5})$$

$$\Rightarrow P_{\text{out}}^{(2)} = \frac{\omega_0^4 p_0^2 n_0}{8\pi \epsilon_0 c^3} = \frac{3n_0}{2} P_{\text{vac}}^{(2)}. \quad (\text{A6})$$

Thus, for a rotating electric point dipole inside a medium with refractive index  $n_0$  enclosed within a 1D DBR cavity

with moderately high quality factor ( $Q \gtrsim 100$ ), the power extracted in the medium (vacuum) outside the cavity converges to a value  $3n_0/2$  times the power radiated by the dipole when placed in vacuum. The exact numerical results agrees well with the above analysis with more than 90% accuracy for a broad range of parameters. We also explicitly state that the above analysis does not make any prediction about the extraction efficiency. Although the extracted power increases linearly with the refractive index of the emitting medium, the extraction efficiency typically goes down due to a steeper increase in the emission into the guided modes of the structure.

[1] A. Hayat, P. Ginzburg, and M. Orenstein, Observation of two-photon emission from semiconductors, *Nat. Photonics* **2**, 238 (2008).

[2] A. Hayat, P. Ginzburg, and M. Orenstein, High-rate entanglement source via two-photon emission from semiconductor quantum wells, *Phys. Rev. B* **76**, 035339 (2007).

- [3] A. Hayat, P. Ginzburg, D. Neiman, S. Rosenblum, and M. Orenstein, Hyperentanglement source by intersubband two-photon emission from semiconductor quantum wells, *Opt. Lett.* **33**, 1168 (2008).
- [4] A. Nevet, A. Hayat, and M. Orenstein, Measurement of Optical Two-Photon Gain in Electrically Pumped Al-GaAs at Room Temperature, *Phys. Rev. Lett.* **104**, 207404 (2010).
- [5] C. Z. Ning, Two-Photon Lasers Based on Intersubband Transitions in Semiconductor Quantum Wells, *Phys. Rev. Lett.* **93**, 187403 (2004).
- [6] Z. Lin and J. Vučković, Enhanced two-photon processes in single quantum dots inside photonic crystal nanocavities, *Phys. Rev. B* **81**, 035301 (2010).
- [7] C. N. Ironside, Two-photon gain semiconductor amplifier, *IEEE J. Quantum Electron.* **28**, 842 (1992).
- [8] A. Hayat, A. Nevet, and M. Orenstein, Electrically Induced Two-Photon Transparency in Semiconductor Quantum Wells, *Phys. Rev. Lett.* **102**, 183002 (2009).
- [9] S. Lloyd, Enhanced sensitivity of photodetection via quantum illumination, *Science* **321**, 1463 (2008).
- [10] V. Giovannetti, S. Lloyd, and L. Maccone, Quantum-enhanced measurements: Beating the standard quantum limit, *Science* **306**, 1330 (2004).
- [11] V. Giovannetti, S. Lloyd, and L. Maccone, Quantum-enhanced positioning and clock synchronization, *Nature (London)* **412**, 417 (2001).
- [12] G. Scarcelli and S. H. Yun, Entangled-photon coincidence fluorescence imaging, *Opt. Express* **16**, 16189 (2008).
- [13] D. Bouwmeester, J.-W. Pan, K. Mattle, M. Eibl, H. Weinfurter, and A. Zeilinger, Experimental quantum teleportation, *Nature (London)* **390**, 575 (1997).
- [14] H. de Riedmatten, I. Marcikic, J. A. W. Van Houwelingen, W. Tittel, H. Zbinden, and N. Gisin, Long-distance entanglement swapping with photons from separated sources, *Phys. Rev. A* **71**, 050302(R) (2005).
- [15] D. Bouwmeester and A. Zeilinger, The physics of quantum information: Basic concepts, in *The Physics of Quantum Information* (Springer, New York, 2000), pp. 1–14.
- [16] B. P. Lanyon, J. D. Whitfield, G. G. Gillett, M. E. Goggin, M. P. Almeida, I. Kassal, J. D. Biamonte, M. Mohseni, B. J. Powell, M. Barbieri, and A. Aspuru-Guzik, Towards quantum chemistry on a quantum computer, *Nat. Chem.* **2**, 106 (2010).
- [17] L.-A. Wu, H. J. Kimble, J. L. Hall, and H. Wu, Generation of Squeezed States by Parametric Down Conversion, *Phys. Rev. Lett.* **57**, 2520 (1986).
- [18] P. G. Kwiat, K. Mattle, H. Weinfurter, A. Zeilinger, A. V. Sergienko, and Y. Shih, New High-Intensity Source of Polarization-Entangled Photon Pairs, *Phys. Rev. Lett.* **75**, 4337 (1995).
- [19] P. G. Kwiat, E. Waks, A. G. White, I. Appelbaum, and P. H. Eberhard, Ultrabright source of polarization-entangled photons, *Phys. Rev. A* **60**, R773 (1999).
- [20] A. Nevet, A. Hayat, and M. Orenstein, Ultrafast pulse compression by semiconductor two-photon gain, *Opt. Lett.* **35**, 3877 (2010).
- [21] M. D. Leistikow, A. P. Mosk, E. Yeganegi, S. R. Huisman, A. Lagendijk, and W. L. Vos, Inhibited Spontaneous Emission of Quantum Dots Observed in a 3D Photonic Band Gap, *Phys. Rev. Lett.* **107**, 193903 (2011).
- [22] S. Noda, M. Fujita, and T. Asano, Spontaneous-emission control by photonic crystals and nanocavities, *Nat. Photonics* **1**, 449 (2007).
- [23] S. Fan, P. R. Villeneuve, and J. D. Joannopoulos, Rate-equation analysis of output efficiency and modulation rate of photonic-crystal light-emitting diodes, *IEEE J. Quantum Electron.* **36**, 1123 (2000).
- [24] A. Yariv, *Quantum Electronics* (John Wiley & Sons, New York, 1989).
- [25] H. J. Carmichael, *Statistical Methods in Quantum Optics I: Master Equations and Fokker-Planck Equations* (Springer Science & Business Media, New York, 1999).
- [26] A. Muller, E. B. Flagg, P. Bianucci, X. Wang, D. G. Deppe, W. Ma, J. Zhang, G. J. Salamo, M. Xiao, and C.-K. Shih, Resonance Fluorescence from a Coherently Driven Semiconductor Quantum Dot in a Cavity, *Phys. Rev. Lett.* **99**, 187402 (2007).
- [27] Y. Fink, J. N. Winn, S. Fan, C. Chen, J. Michel, J. D. Joannopoulos, and E. L. Thomas, A dielectric omnidirectional reflector, *Science* **282**, 1679 (1998).
- [28] J. N. Winn, Y. Fink, S. Fan, and J. D. Joannopoulos, Omnidirectional reflection from a one-dimensional photonic crystal, *Opt. Lett.* **23**, 1573 (1998).
- [29] I. Nusinsky and A. A. Hardy, Omnidirectional reflection in several frequency ranges of one-dimensional photonic crystals, *Appl. Opt.* **46**, 3510 (2007).
- [30] J. D. Joannopoulos, S. G. Johnson, J. N. Winn, and R. D. Meade, *Photonic Crystals: Molding the Flow of Light*, 2nd ed. (Princeton University Press, Princeton, NJ, 2011).
- [31] G. Bastard, E. E. Mendez, L. L. Chang, and L. Esaki, Exciton binding energy in quantum wells, *Phys. Rev. B* **26**, 1974 (1982).
- [32] R. C. Miller, D. A. Kleinman, W. T. Tsang, and A. C. Gossard, Observation of the excited level of excitons in GaAs quantum wells, *Phys. Rev. B* **24**, 1134 (1981).
- [33] R. Baets, P. Bienstman, and R. Bockstaele, Basics of dipole emission from a planar cavity, in *Confined Photon Systems* (Springer, New York, 1999), pp. 38–79.
- [34] L. Polerecký, J. Hamrle, and B. D. MacCraith, Theory of the radiation of dipoles placed within a multilayer system, *Appl. Opt.* **39**, 3968 (2000).
- [35] H. D. N. H. Benisty, R. Stanley, and M. Mayer, Method of source terms for dipole emission modification in modes of arbitrary planar structures, *J. Opt. Soc. Am. A* **15**, 1192 (1998).
- [36] Y. Xu, J. S. Vučković, R. K. Lee, O. J. Painter, A. Scherer, and A. Yariv, Finite-difference time-domain calculation of spontaneous emission lifetime in a microcavity, *J. Opt. Soc. Am. B* **16**, 465 (1999).